Tunable Edelstein effect in the intrinsic two-dimensional ferroelectric metal $PtBi_2$

Weiyi Pan [1,*] and Jaroslav Fabian [1,2]
[1]*Institute for Theoretical Physics, University of Regensburg, 93040 Regensburg, Germany*
[2]*Halle-Berlin-Regensburg Cluster of Excellence CCE, Halle, Germany*

(Received 25 January 2026; revised 30 March 2026; accepted 6 April 2026; published 22 April 2026)

The Edelstein effect, which enables charge-to-spin conversion and is therefore highly promising for future spintronic devices, can be realized and nonvolatilely manipulated in ferroelectric materials owing to their broken inversion symmetry and switchable polarization states. To date, most ferroelectric systems reported to exhibit the Edelstein effect are semiconductors, requiring extrinsic doping for functionality. In contrast, the Edelstein effect has rarely been reported in metallic ferroelectric systems, where doping is unnecessary. Using first-principles calculations, we predict that a pronounced Edelstein effect can be realized in the recently proposed intrinsic two-dimensional ferroelectric metal $PtBi_2$ monolayer, where the sign of the Edelstein coefficient is coupled to the direction of ferroelectric polarization through the polarization-switching-induced reversal of spin textures, thereby enabling nonvolatile control of charge-spin conversion. The Edelstein effect reaches a magnitude of $2.32 \times 10^{10}\hbar/(\mathrm{A\,cm})$, which is relatively large among those of previously reported ferroelectric systems. Microscopically, the Edelstein effect in a $PtBi_2$ monolayer originates from competing contributions of inner Rashba-like electron pockets and outer hole pockets with opposite signs; an upward shift of the Fermi level alters their balance and can reverse the sign of the Edelstein effect. Upon the application of biaxial strain, the Fermi-surface electronic structure is strongly modified, resulting in a pronounced change in the Edelstein effect: A 2% compressive strain suppresses the Edelstein effect by about 50%. Our results not only identify a promising material platform for tunable charge-spin conversion but also provide insights into the functional potential of metallic ferroelectric systems.

DOI: 10.1103/j5s5-m7j5

I. INTRODUCTION

The Edelstein effect (EE) [1,2], which refers to the conversion of an applied charge current into a nonequilibrium spin accumulation in the presence of spin-orbit coupling (SOC), plays a central role in the development of spin-orbit-torque devices and spin-based logic architectures. Quantitatively, the EE can be described by a susceptibility tensor χ, which links the induced spin density $\delta\mathbf{S}$ to the applied electric field $\mathbf{E}$ [2,3]: $\delta S_i = \chi_{ij} E_j$. Such an EE, which typically originates from noncollinear spin textures in k space generated by SOC, requires broken inversion symmetry and would experience a sign reversal upon the spatial inversion operation. Therefore, achieving a sizable EE in practical material systems hinges on simultaneously breaking inversion symmetry and ensuring the presence of strong SOC.

Previously, the EE has been investigated in a variety of inversion-asymmetric systems, including two-dimensional (2D) van der Waals heterostructures [4–8], metal interfaces [9,10], 2D electron gases at oxide interfaces [11–14], surfaces of topological insulators [15–17], and chiral nanowires [18–20]. In these systems, the spin textures can be further tuned through voltage gating [19] or twisting [6,8], thereby modulating the magnitude of the EE.

Ferroelectric materials offer a promising platform for studying the EE [21–27]. In ferroelectric systems, the absence of inversion symmetry naturally allows the noncollinear k-space spin textures and the EE to occur. Moreover, by switching the direction of electric polarization, both the helicity of spin textures and the sign of EE coefficient can be inverted, which provides opportunities for designing nonvolatile and electrically controllable device functionalities. Previously, the ferroelectric-controllable EE was explored in several ferroelectric systems, such as GeTe [21,27], In_2Se_3 [23], the graphene/In_2Se_3 heterostructure [28], and $CsGeX_3$ (X = I, Br, Cl) [26]. However, most observed ferroelectric materials are insulating, making it necessary to dope them into a conductive regime to realize the EE and thus increase the burden of the experiment. In contrast, emerging ferroelectric metals, in which ferroelectricity coexists with metallicity, offer a new route toward achieving switchable EE without the need for doping [29–31]. Nevertheless, intrinsic ferroelectric metals, particularly those in the 2D limit that are advantageous for both highly integrated electronic applications and higher tunability for potential functionalities, remain largely elusive. Therefore, more candidates of intrinsic 2D ferroelectric metals with an effective EE are highly desired both theoretically and experimentally.

Recently, monolayer $PtBi_2$ was proposed as a rare example of an intrinsic 2D ferroelectric metal [32] (see Fig. 1). It has been predicted that monolayer $PtBi_2$ can be exfoliated from experimentally accessible bulk trigonal $PtBi_2$ [33–36] with

*Contact author: Weiyi.Pan@physik.uni-regensburg.de

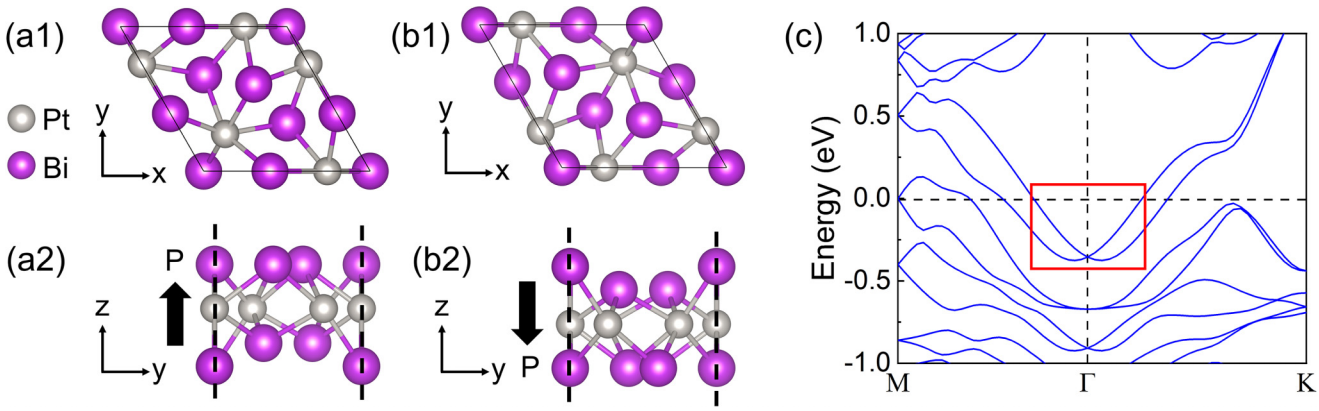

FIG. 1. The atomic structure of monolayer $PtBi_2$ with the polarization (a) upward ($P_\uparrow$ state) and (d) downward ($P_\downarrow$ state). (a1) and (b1) show the top views, while (a2) and (b2) show the side views. (c) The band structure of monolayer $PtBi_2$ with polarization upward; the band structure of $PtBi_2$ with polarization downward is identical. The Rashba-like bands forming electron pockets near the Γ point are indicated in the box.

moderate exfoliation energy [32], and it also exhibits robust metallicity together with reversible ferroelectric polarization originating from a distorted monolayer structure, featuring a moderate switching barrier and a considerable polarization magnitude [32]. Moreover, the strong SOC inherent in $PtBi_2$ gives rise to a topologically nontrivial band structure [32], which in turn leads to an enhanced shift-current conductivity desirable for future photovoltaic applications [37]. This unique combination of intrinsic ferroelectricity, metallicity, and strong SOC in monolayer $PtBi_2$ makes it an excellent candidate for realizing intrinsic and switchable EE, which motivates us to conduct a detailed investigation of its EE performance, tunability, and the microscopic mechanisms underlying it.

In this work, we systematically investigate the tunable EE in monolayer $PtBi_2$. Based on first-principles calculations, we demonstrate that a considerable EE can intrinsically exist in this material. Such an EE reaches a magnitude of $2.32 \times 10^{10}\hbar/(\mathrm{A\,cm})$, which represents a relatively large value among previously reported ferroelectric systems. With the reversal of the ferroelectric polarization of monolayer $PtBi_2$, the sign of the EE coefficient also switches. Microscopically, the EE arises from combined contributions of the inner Rashba-like electron pockets and the outer hole pockets on the Fermi surface, which may compete with one another. Furthermore, the EE in monolayer $PtBi_2$ can be additionally tuned by applying biaxial strain. Our findings not only provide insights into the functional potential of intrinsic ferroelectric metals but also broaden the range of candidate materials for charge-spin conversion in future spintronic devices.

II. METHODS

Our first-principles calculations are performed using the QUANTUM ESPRESSO package [38]. In our work, the Perdew-Burke-Ernzerhof [39] exchange-correlation functional and projector augmented-wave [40] potentials are employed. Both structural relaxation and self-consistent calculations use a $9 \times 9 \times 1k$-point mesh, with energy cutoffs of 500 Ry for the charge density and 60 Ry for the wave functions. Structural relaxations are carried out using scalar-relativistic pseudopotentials and the quasi-Newton algorithm until all components of the forces are smaller than 3×10^{-4} Ry/a_0, where a_0 is the Bohr radius. Self-consistent calculations are then performed with fully relativistic pseudopotentials to account for SOC. A vacuum spacing of 28 Å is applied in all simulations to eliminate interactions between periodic images in the slab geometry.

After the density functional theory calculations, we construct the Wannier Hamiltonian of our system using the WANNIER90 [41] code. For the Wannierization procedure, the d orbitals of Pt and the p orbitals of Bi are selected as the projection basis. Based on the resulting Wannier Hamiltonian, we employ the WANNIERTOOLS [42] package to compute the Fermi surface and the corresponding spin textures. In addition, we use the LINRES [43] code to evaluate the EE via the Kubo formula. Specifically, we consider the linear response of spin polarization to an external electric field, expressed as $\delta\mathbf{S} = \chi\mathbf{E}$, where $\delta\mathbf{S}$ is the induced spin polarization, $\mathbf{E}$ is the electric field, and χ is the response tensor in nonmagnetic systems, which can be written as [44–46]

$$\chi_{ij} = -\frac{e\hbar}{\pi N}\sum_{\mathbf{k},m,n}\frac{\Gamma^2\mathrm{Re}(\langle n\mathbf{k}|\hat{S}_i|m\mathbf{k}\rangle\langle m\mathbf{k}|\hat{v}_j|n\mathbf{k}\rangle)}{[(E_f-\epsilon_{n\mathbf{k}})^2+\Gamma^2][(E_f-\epsilon_{m\mathbf{k}})^2+\Gamma^2]}. \quad (1)$$

Here, e is the elementary charge, n and m denote band indices, $\mathbf{k}$ is the Bloch wave vector, E_F is the Fermi energy, $\hat{v}$ is the velocity operator, $\hat{S}$ is the spin operator, $\epsilon_{n\mathbf{k}}$ is the eigenvalue, N is the total number of k points used to sample the Brillouin zone, and Γ is the disorder parameter, which is related to the relaxation time τ through $\tau = \hbar/2\Gamma$. It is worth noting that the EE originates mainly from the electronic states on the Fermi surface [47]. This becomes evident when Γ is small since in this case the above expression can be approximated as [44]

$$\chi_{ij} = -\frac{e\hbar}{2\Gamma N}\sum_{\mathbf{k},n}\delta(\epsilon_{nk}-E_F)\langle n\mathbf{k}|\hat{S}_i|n\mathbf{k}\rangle\langle n\mathbf{k}|\hat{v}_j|n\mathbf{k}\rangle, \quad (2)$$

where the $\delta(\epsilon_{n\mathbf{k}} - E_F)$ part explicitly indicates that states at the Fermi level will dominate the EE. Here, we set $\Gamma = 10$ meV, which roughly corresponds to a typical <100 fs

scattering rate (broadening) while remaining much smaller than interband separations. Finally, a $400 \times 400 \times 1k$-point mesh is used to obtain the converged EE coefficient.

III. RESULTS AND DISCUSSION

Monolayer $PtBi_2$ crystallizes in space group 157 (the C_{3v} point group). It consists of a Pt layer sandwiched between two Bi layers, forming a distorted structure with nine atoms in the unit cell, which is shown in Fig. 1. The in-plane lattice constant is calculated to be 6.56 Å, which is consistent with previous studies [32,33]. Such monolayer $PtBi_2$ was reported to have two ferroelectric ground states with opposite electric polarizations, namely, the $P_\uparrow$ and $P_\downarrow$ states [see Figs. 1(a) and 1(b)], which are connected by the inversion operation $\mathcal{P}$ and are electrically switchable [32]. In the $P_\uparrow$ ($P_\downarrow$) configuration, the top (bottom) Bi layer lies in a single plane, whereas the Bi atoms in the bottom (top) layer do not lie in the same plane. Such a structural arrangement breaks both inversion symmetry $\mathcal{P}$ and mirror symmetry $\mathcal{M}_z$, which allows the existence of perpendicular electric polarization [32].

To gain further insights, we evaluate the electronic band structure of monolayer $PtBi_2$, as shown in Fig. 1(c). Several energy bands cross the Fermi level, indicating pronounced metallic behavior. Notably, two bands intersect the Fermi level in the vicinity of the Γ point, forming two electron pockets. These bands are degenerate at the Γ point but split upon moving away from it, exhibiting a characteristic Rashba-type band splitting that could potentially be observed experimentally via angle-resolved photoemission spectroscopy [48,49]. Quantitatively, the Rashba effect can be described by the Rashba parameter $\alpha_R = 2E_R/k_R$, where E_R and k_R denote the Rashba splitting energy and momentum offset, respectively [48]. The calculated Rashba parameter is $\alpha_R = 1.10\,\text{eV Å}$, which is considerable compared with several representative 2D Rashba systems, such as metal surface states [50,51], 2D electron gases [12,52], and 2D heterostructures [48,53]. Note that such Rashba splitting is usually expected to make a significant contribution to the EE [2,54]. In addition to the two electron pockets near the Γ point, another band crosses the Fermi level near the M point, giving rise to hole pockets on the Fermi surface. Since monolayer $PtBi_2$ exhibits both inversion-symmetry breaking and strong SOC, the presence of the EE is naturally expected. Moreover, in ferroelectric systems, the sign of the EE coefficient can be reversed through ferroelectric switching, which may also occur in monolayer $PtBi_2$. Based on symmetry considerations, space group 157 (the C_{3v} point group) allows only two nonzero components of the EE tensor, $\chi_{yx} = -\chi_{xy}$, to exist in monolayer $PtBi_2$. By computing the χ_{yx} component of the EE coefficient as a function of the chemical potential and polarization direction (see Fig. 2), one finds that reversing the polarization indeed switches the sign of the EE coefficient. Such a sign reversal of the Edelstein coefficient can be understood from the viewpoint of symmetry: From the definition of the Edelstein effect $\delta\mathbf{S} = \chi\mathbf{E}$, in which $\delta\mathbf{S}$ is a spatial-inversion-even axial vector and $\mathbf{E}$ is a spatial-inversion-odd polar vector, one can see that spatial inversion would reverse the sign of $\mathbf{E}$ but leave $\delta\mathbf{S}$ unchanged, thereby leading to the sign change of χ. Note that such a ferroelectric-switchable EE was reported

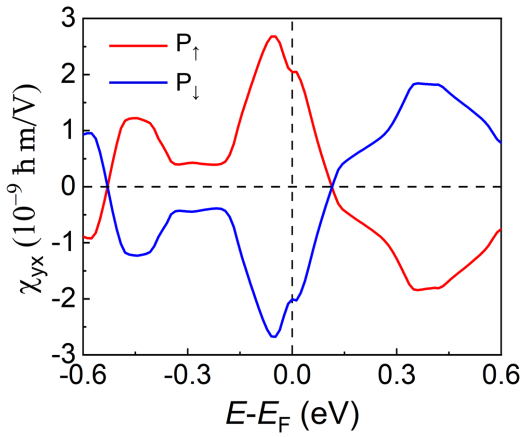

FIG. 2. Calculated EE coefficient in monolayer $PtBi_2$. The curves corresponding to opposite polarization states $P_\uparrow$ and $P_\downarrow$ are labeled in red and blue, respectively.

previously in ferroelectric semiconductors [23,26]. In contrast, for metallic ferroelectrics, a finite EE can exist without the need for additional doping. Although a previous theoretical study discussed this effect in $1T'$-WTe_2 [24], more reports of the EE in ferroelectric metals remain scarce and are therefore highly desirable. For the $P_\uparrow$ state, the magnitude of the EE at the Fermi level is approximately $2.0 \times 10^{-9}\hbar\,\text{m/V}$. This value is comparable to that of 2D Rashba electron gases [11,12] and 2D heterostructures [55] but 1 order of magnitude larger than those found in typical p-wave magnets such as $LuFeO_3$ [56] and CeNiAsO [57]. After one normalizes by the longitudinal conductivity and considers an effective monolayer thickness of 4 Å, the EE coefficient reaches a magnitude of $2.32 \times 10^{10}\hbar/(\text{A cm})$ (see Appendix A for more details), which means that a charge current of 100 A/cm^2 will generate a spin density of $2.32 \times 10^{12}/\text{cm}^3$ (or $0.93 \times 10^5/\text{cm}^2$ after it is normalized to two dimensions). With such a magnitude of the EE, with the addition of a current of up to 10^8 A/cm^2 to monolayer $PtBi_2$, the spin polarization of the system can reach 0.01% (see Appendix B). Note that our calculated normalized EE coefficient is relatively large compared with those of previously calculated ferroelectric systems, which typically fall within the range of 10^9–$10^{10}\hbar/(\text{A cm})$ [23,24,26] (see also Appendix D). It is also worth noting that the maximum value of the EE coefficient occurs at $E_F = -0.05$ eV, which lies near the Fermi level and can, in principle, be accessed by gating [58]. Meanwhile, when the Fermi level shifts toward higher energies, the EE for the $P_\uparrow$ ($P_\downarrow$) state decreases (increases) monotonically and changes sign at $E_F = 0.2\,\text{eV}$.

Since the EE is dominated by Fermi-surface states [47], it is essential to examine how the electronic states evolve with respect to the Fermi level, so that the microscopic origin of EE can be further unveiled. For this purpose, we evaluate the Fermi surfaces and corresponding spin textures at different chemical potentials for the $P_\uparrow$ state of monolayer $PtBi_2$, as shown in Fig. 3. As clearly seen in Fig. 3(b), at $E_F = 0$ eV, the two electron pockets near the Γ point exhibit Rashba-like spin textures with opposite helicity. In addition, six separate hole pockets appear away from the Γ point. When the Fermi level is shifted downward to $E_F = -0.05$ eV [see Fig. 3(a)], the

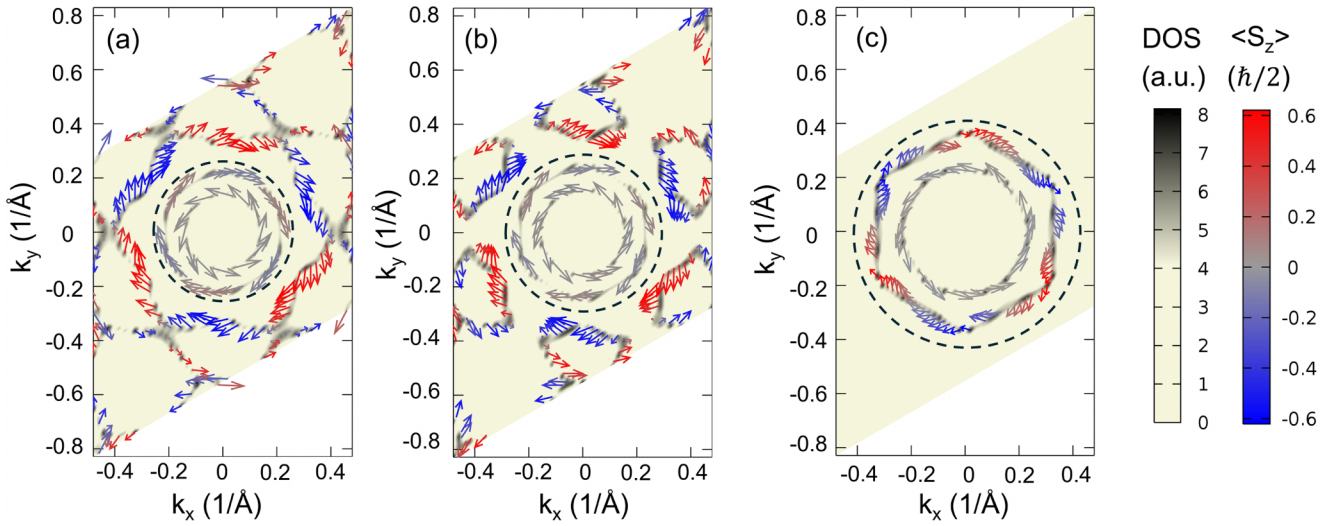

FIG. 3. The Fermi surface states as well as the corresponding spin textures for the $P_\uparrow$ state of monolayer $PtBi_2$ at (a) $E_F = -0.05$ eV, (b) $E_F = 0$ eV, and (c) $E_F = 0.2$ eV. The background color shows the spectral density of electronic states on the Fermi surface, expressed in arbitrary units. The arrows indicate the direction and magnitude of the in-plane spin expectation values for these Fermi surface states. The color of the arrow represents the expectation value of out-of-plane spin components. The states from inner electron pockets near the Γ point are circled, while the states outside of the circle are from outer hole pockets.

spin textures of the inner electron pockets remain qualitatively unchanged, although their areas shrink. Meanwhile, the outer hole pockets expand and begin to merge. This not only makes the outer hole bands away from the Γ point more pronounced but also leads to the formation of a closed wrapped hole pocket with a Rashba-like spin texture. This behavior arises because lowering the Fermi level allows additional hole bands to occur at the Fermi surface. In contrast, when the Fermi level is shifted upward to $E_F = 0.2$ eV [see Fig. 3(c)], the hole pockets shrink and eventually disappear, while the electron pockets with Rashba-like spin textures expand. Meanwhile, the outer electron pocket also develops a slight warping distortion, which is compatible with the C_{3v} symmetry of the system [59,60]. The above analysis applies to the $P_\uparrow$ state of monolayer $PtBi_2$. For the $P_\downarrow$ state, while the shape of the Fermi surface at each evaluated energy remains unchanged, the directions of the spin textures are reversed, which is not shown here. The above variation of the Fermi level modifies the distribution of electronic states on Fermi surface and thus alters their contribution to the EE. To gain deeper insights, we rewrite the EE as a sum of k-resolved terms:

$$\chi_{yx} = \frac{(2\pi)^3}{VN} \sum_k \chi_{yx}(E_F, \mathbf{k}), \tag{3}$$

where V and N are the volume of the unit cell and the total number of k points used to sample the Brillouin zone, respectively. The distribution of the k-resolved EE coefficient $\chi_{yx}(E_F, \mathbf{k})$ for the $PtBi_2$ monolayer in the $P_\uparrow$ state is shown in Fig. 4. As seen at $E_F = 0$ eV [see Fig. 4(b)], the two inner electron pockets contribute oppositely to the

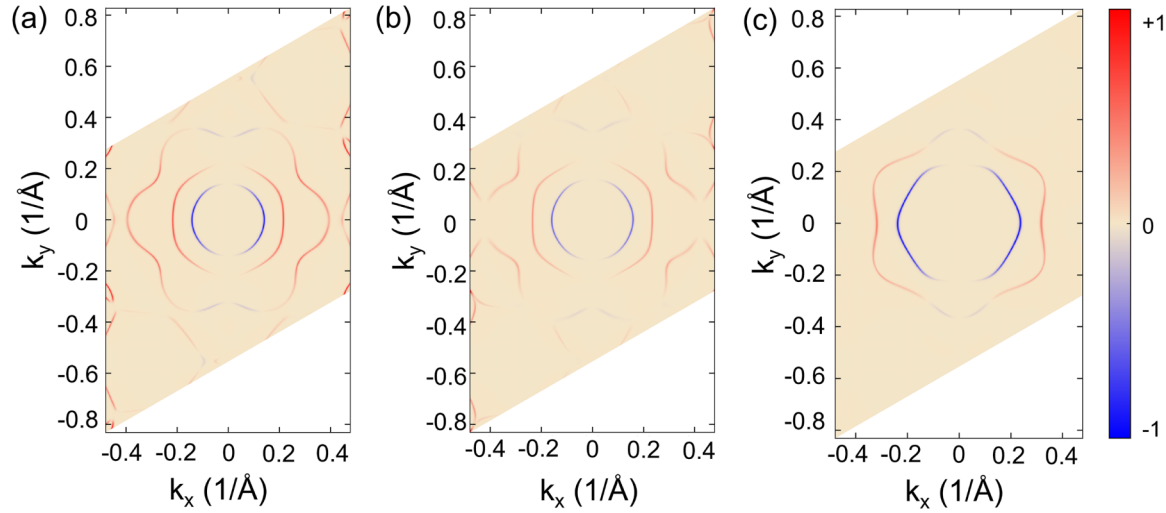

FIG. 4. The $\mathbf{k}$-resolved EE coefficient $\chi_{yx}(E_F, \mathbf{k})$ for the $P_\uparrow$ state of monolayer $PtBi_2$ at (a) $E_F = -0.05$ eV, (b) $E_F = 0$ eV, and (c) $E_F = 0.2$ eV. Red and blue denote the positive and negative values of $\chi_{yx}(E_F, \mathbf{k})$, respectively, which have been normalized to the maximum value.

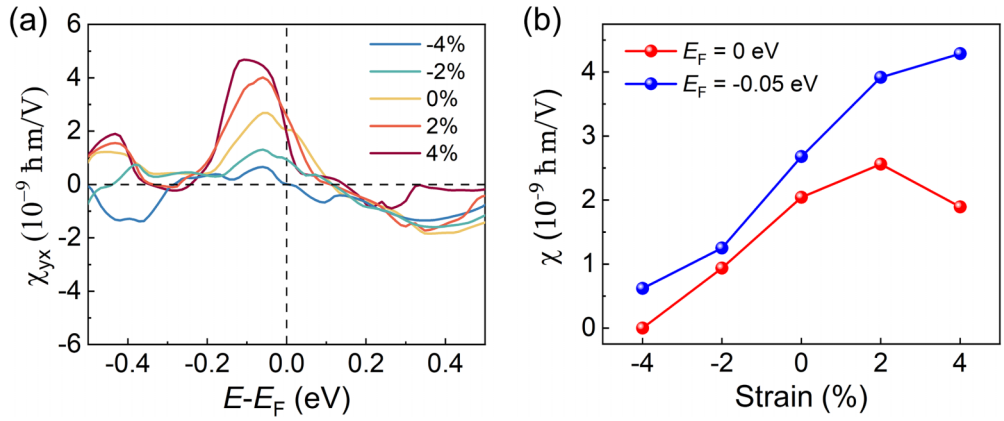

FIG. 5. (a) The EE coefficient for the $P_\uparrow$ state of monolayer $PtBi_2$ under different biaxial strain levels. (b) The values of the EE coefficient at $E_F = 0$ eV and $E_F = -0.05$ eV as a function of biaxial strain level.

current-induced spin polarization, which is in line with their opposite Rashba-like spin textures. Meanwhile, the outer hole pockets generally contribute positively to the EE. Therefore, the total EE in monolayer $PtBi_2$ arises from the interplay between the inner electron pockets near the Γ point and the outer hole pockets. When the Fermi level is shifted downward to $E_F = -0.05$ eV [see Fig. 4(a)], the contribution from the inner electron pockets remains qualitatively unchanged, whereas more hole states with positive contributions appear on the Fermi surface, thereby positively enhancing the total EE. Conversely, when the Fermi level is shifted upward, the outer hole pockets gradually shrink and eventually disappear at $E_F = 0.2$ eV [see Fig. 4(c)]. In this situation, the EE is dominated by the two inner electron pockets, whose combined contribution is negative. As the outer hole pockets are responsible for the positive component of the EE, their disappearance suppresses the positive contribution, leading to a monotonic decrease of the total EE and ultimately causing its sign reversal as the Fermi level increases from 0 to 0.2 eV. Based on the above analysis, we conclude that the EE in monolayer $PtBi_2$ is affected by the delicate interplay between inner electron pockets and outer hole pockets. Moreover, by tuning the Fermi level, which can be experimentally achieved through slight doping or gating [58], one can modulate the competition between contributions from the inner electron pockets and the outer hole pockets, thereby controlling the Edelstein effect in monolayer $PtBi_2$.

Besides ferroelectric switching, the EE in realistic ferroelectric systems can also be manipulated by applying moderate strain [26], which can be achieved by growing the sample on an appropriate substrate where the lattice mismatch between the substrate and the sample induces and sustains strain [61–63]. This naturally raises the question of whether the EE in monolayer $PtBi_2$ is tunable by strain. To address this, we evaluate the EE coefficient in monolayer $PtBi_2$ as a function of biaxial strain, as shown in Fig. 5(a). It is evident that the EE coefficient is strongly affected by strain. For example, tensile strain generally enhances the EE across the entire evaluated energy range, whereas compressive strain suppresses it. By plotting the EE coefficient as a function of strain at $E_F = 0$ eV, which leads to the intrinsic value of the EE without the need of doping, and at $E_F = -0.05$ eV, where the pristine monolayer exhibits its maximum EE [see Fig. 5(b)], one finds that strain induces a substantial variation in the EE. Specifically, for $E_F = 0$ eV, tensile strain does not lead to much change in the EE coefficient, while compressive strain strongly suppresses the EE. To be specific, a compressive strain of -2% will suppress the EE by about 50%, while adding a larger compressive strain of -4% will make the EE decrease to roughly zero. On the other hand, for $E_F = -0.05$ eV, a moderate tensile strain of 4% enhances the EE to about 150% of its unstrained value, while a compressive strain of -4% reduces it to roughly 30% of its unstrained value. Microscopically, these strain-induced variations of the EE arise from changes in the electronic states on the Fermi surface, which in turn modify their contributions to the EE (see Appendix E). These results highlight the potential of monolayer $PtBi_2$ as a platform for strain-tunable charge-to-spin conversion.

IV. CONCLUSIONS

In conclusion, based on first-principles calculations, we explored the EE in the intrinsic 2D ferroelectric metal $PtBi_2$. We found that the $PtBi_2$ monolayer exhibits sizable intrinsic EE coefficients, whose signs can be reversed through ferroelectric switching, thereby enabling nonvolatile electrical control of charge-spin conversion. Microscopically, the EE originates from the interplay between the inner Rashba-like electron pockets and the outer hole pockets on the Fermi surface. This interplay can be altered by shifting the Fermi level, thereby leading to a sign change of the EE when the Fermi level is shifted upward. Furthermore, by adding strain to the system, the electronic state on the Fermi surface is strongly modified, thereby leading to a pronounced variation in the EE. Note that although the ferroelectric-switching-induced sign reversal of the Edelstein effect follows directly from symmetry considerations, sizable and tunable intrinsic Edelstein effects in metallic ferroelectric systems without the need for additional doping are scarce, which emphasizes the importance of our results. We believe that our results not only broaden the material candidates for effective charge-spin conversion in low-dimensional systems but also pave the way for nonvolatile, electrically controllable spintronic devices.

ACKNOWLEDGMENTS

This project was supported by the European Union Graphene Flagship project 2DSPIN-TECH (Grant Agreement No. 101135853) and SFB 1277 (Project-ID 314695032).

DATA AVAILABILITY

The data that support the findings of this article are not publicly available upon publication because it is not technically feasible and/or the cost of preparing, depositing, and hosting the data would be prohibitive within the terms of this research project. The data are available from the authors upon reasonable request.

APPENDIX A: CONVERSION BETWEEN EDELSTEIN COEFFICIENTS WITH DISTINCT UNITS

Besides the original Edelstein coefficient χ_{ij} defined as $\delta S_i = \chi_{ij} E_j$ used in the main text, which denotes the spin angular momentum $\hbar$ in a single unit cell induced by the electric field (V/m) and has units of $\hbar$ m/V, one can also define a normalized current-induced Edelstein coefficient χ'_{ij} with $\delta S_i = \chi'_{ij} J_j$ [20,64] which denotes the three-dimensional volume density of spin angular momentum ($\hbar/\mathrm{cm}^3$) induced by current density ($\mathrm{A/cm}^2$) and has units of $\hbar/(\mathrm{A\,cm})$.

Since the electric current component J_i can be related to the electric field E_i by $J_i = \sigma_{ii} E_i$, where σ_{ii} is the longitudinal conductivity of the system, χ_{ij} can thus be converted into χ'_{ij} with the following expression:

$$\chi'_{ij} = \chi_{ij}/(V\sigma_{ii}) \tag{A1}$$

where V is the effective volume of the system. Here, σ_{ii} can be calculated using the Kubo formula implemented in the LINRES code [43]:

$$\sigma_{ii} = \frac{e^2\hbar}{\pi V N} \sum_{\mathbf{k},m,n} \frac{\Gamma^2 \mathrm{Re}(\langle n\mathbf{k}|\hat{v}_i|m\mathbf{k}\rangle\langle m\mathbf{k}|\hat{v}_i|n\mathbf{k}\rangle)}{[(E_f-\epsilon_{n\mathbf{k}})^2+\Gamma^2][(E_f-\epsilon_{m\mathbf{k}})^2+\Gamma^2]}. \tag{A2}$$

Here, e is the elementary charge, n and m denote band indices, $\mathbf{k}$ is the Bloch wave vector, E_F is the Fermi energy, $\hat{v}$ is the velocity operator, $\hat{S}$ is the spin operator, $\epsilon_{n\mathbf{k}}$ is the eigenvalue, V is the volume of the unit cell after the effective thickness of the two-dimensional monolayer is considered, N is the total number of k points used to sample the Brillouin zone, and $\Gamma = 10$ meV is the disorder parameter. Based on the calculated longitude conductivity and considering a monolayer thickness of about 4 Å, we arrive at a normalized EE of $\chi'_{yx} = -\chi'_{xy} = 2.32 \times 10^{10}\hbar/(\mathrm{A\,cm})$. Note that the magnitude of the normalized Edelstein effect is largely independent of the Γ broadening and can thus serve as a reliable reference value.

APPENDIX B: ESTIMATING THE CURRENT-INDUCED SPIN POLARIZATION

The spin polarization in a two-dimensional system is defined as $p = \delta\mathbf{S}/n$, where $\delta\mathbf{S}$ is the current-induced spin density under a specific current and can be obtained through the calculated EE coefficient and n is the carrier density. n can be estimated via Drude's formula, $\sigma = ne^2\tau/m_e$, where m_e is the mass of an electron and $\tau = \hbar/2\Gamma$ is the relaxation time. Based on the longitudinal conductivity calculated with the Kubo formula in Eq. (A2) and normalizing the calculated density to two dimensions, we can arrive at $n = 2.5 \times 10^{14}\ \mathrm{cm}^{-2}$. With such an estimated n, we can predict the current-induced spin polarization for the given electrical current density stated in the main text.

APPENDIX C: ROLE OF THE SPIN HALL EFFECT

Besides the Edelstein effect, another intriguing charge-to-spin conversion phenomenon is the spin Hall effect [65], which denotes the current-induced intrinsic spin current in the material. In ferroelectric systems, the spin Hall effect is also widely studied [66–68], which provides new routes for nonvolatile manipulation of charge-spin conversion. The spin Hall effect can be expressed as $J^i_j = \sigma^i_{jk} E_k$, where J^i_j denotes the spin current flowing along j carrying spin polarization along i, while σ^i_{jk} denotes the spin Hall conductivity. In our current system (monolayer $PtBi_2$), because we consider the contraint of C_{3v} symmetry as well as its two-dimensional nature, the only nonzero spin Hall conductivity components at the Fermi level are $\sigma^z_{xy} = -\sigma^z_{yx} = 319(\hbar/e)\,(\mathrm{S/cm})$, which is calculated using Kubo's formula implemented in the WANNIER90 code [69]. This indicates that when an electric current is applied along the $+x$ ($+y$) direction in the $PtBi_2$ monolayer, a transverse spin current is generated along the $+y$ ($+x$) direction, carrying spin polarization along the $+z$ direction. Note that in an ideal two-dimensional crystal, spin currents induced by the spin Hall effect are expected to flow uniformly throughout the material and are therefore not intrinsically converted into a net nonequilibrium spin polarization within the bulk.

On the other hand, at the boundary of the system, the spin current would experience scattering, thereby leading to the local accumulation of spin polarization. To roughly estimate it, we note that the spin current density is related to the difference of the angular moment carried by the spin-polarized current:

$$J_s = \frac{\hbar}{2e}(J_\uparrow - J_\downarrow). \tag{C1}$$

Meanwhile, the spin-polarized current is related to the chemical potential gradient of spin-polarized electrons, which can be expressed as $J_\uparrow = \frac{\sigma}{e}\nabla\mu_\uparrow$ and $J_\downarrow = \frac{\sigma}{e}\nabla\mu_\downarrow$; we can naturally express the spin current density as a function of the gradient of the spin chemical potential [70]:

$$J_s = \frac{\hbar}{4e^2}\sigma\nabla(\mu_\uparrow - \mu_\downarrow), \tag{C2}$$

TABLE I. Comparation of the Edelstein coefficient magnitudes $|\chi'_{yx}|$ across different ferroelectric systems. Note that for the $PtBi_2$ monolayer and 2D WTe_2 bilayer, which are ferroelectric metals, the Edelstein effect is calculated at the Fermi level. For the other systems, which are insulators, the maximum value of the Edelstein coefficient in the valence band is shown. The units of the Edelstein coefficient are $10^{10}\hbar/(\mathrm{A\,cm})$.

Material	Edelstein Coefficient	Ref.
$PtBi_2$	2.32	This Work
$CsGeI_3$	0.79	[26]
$CsGeBr_3$	0.53	[26]
$CsGeCl_3$	0.26	[26]
GeTe	1.31	[23]
In_2Se_3	1.40	[23]
WTe_2 bilayer	1.40	[24]

TABLE II. Comparation of the spin Hall conductivity magnitudes $|\sigma^z_{xy}|$ for different ferroelectric systems. The units of spin Hall conductivity are $10^2(\hbar/e)\,(\mathrm{S/cm})$. Note that for the α-Bi/SnSe heterostructure, we use an effective thickness of 10 Å, and the spin Hall effect coefficient is obtained at the Fermi level. However, for the other systems, which are insulators, the magnitude of the spin Hall effect is obtained by taking the maximum value at the valence band.

Material	Spin Hall Conductivity	Ref.
$PtBi_2$	3.19	This Work
α-Bi/SnSe	∼0.4	[66]
GeTe	∼8	[68]
Three-dimensional SnTe	∼7	[68]
2D SnTe	∼3	[67]

where σ denotes the electric conductivity. Note that $\mu_\uparrow - \mu_\downarrow$, which denotes the difference in the chemical potential of electrons with distinct spin polarization, is related to the nonequilibrium spin density as

$$\delta S = \frac{\hbar}{4} N(E_F)(\mu_\uparrow - \mu_\downarrow), \tag{C3}$$

where $N(E_F)$ is the electron density of states at the Fermi level, which can be obtained with first-principles calculations. In a spin diffusion regime, such as the boundary, one can approximately get

$$\nabla(\mu_\uparrow - \mu_\downarrow) = \frac{\mu_\uparrow - \mu_\downarrow}{L_s}, \tag{C4}$$

where L_s is the spin diffusion length. Meanwhile, we note that $J_s = \sigma_{\mathrm{SH}} E$ and $\delta S = \chi_{\mathrm{eff}} E$, where σ_{SH} and χ_{eff} denote the spin Hall conductivity and effective Edelstein effect coefficient, respectively. Then we can arrive at the expression for the effective Edelstein effect caused by spin diffusion:

$$\chi_{\mathrm{eff}} = \frac{e^2 N(E_F) L_s \sigma_{\mathrm{SH}}}{\sigma}. \tag{C5}$$

Based on the above expression and our calculated spin Hall coefficients, if we assume the spin diffusion length lies in the range of 1 to 10 nm, which is a typical magnitude at the boundary of a two-dimensional system, the effective Edelstein effect of monolayer $PtBi_2$ caused by extrinsic scattering of the spin current at the boundary will be in the range of 10^{-11} to $10^{-10}\hbar$ m/V.

Although a nonzero local spin-current-induced effective Edelstein effect can be obtained in a diffusion regime, such as the boundary of a material, we argue that the spin polarization induced by the spin current exhibits opposite signs at opposite boundaries of the same system. As a result, the net contribution over the entire system cancels out to zero. This behavior contrasts with the conventional Edelstein effect, which enables a globally nonzero spin polarization to develop under an applied current. Furthermore, based on symmetry considerations, in our C_{3v}-symmetric system, reversing the ferroelectric polarization (equivalent to applying an inversion operation) does not change the sign of σ^z_{xy} or σ^z_{yx}. Based on these arguments, we conclude that the spin Hall effect does not dominate the ferroelectric-reversible intrinsic current-induced spin polarization in the $PtBi_2$ monolayer.

APPENDIX D: COMPARISON OF THE EDELSTEIN EFFECT AND SPIN HALL EFFECT AMONG DISTINCT FERROELECRIC SYSTEMS

In Tables I and II, we summarize the calculated Edelstein coefficients and spin Hall conductivities for various ferroelectric materials reported in previous studies, together with those obtained for our system. It can be seen that the Edelstein coefficients of the $PtBi_2$ monolayer are relatively large compared to those for other ferroelectric systems, while the spin Hall effect is comparable with those of other selected ferroelectric systems. This highlights that the $PtBi_2$ monolayer serves as an excellent platform for investigating charge-spin conversion phenomena in two-dimensional systems.

APPENDIX E: THE EFFECT OF STRAIN ON THE FERMI SURFACE, SPIN TEXTURES, AND EE EFFECT

Below, we present the spin textures of the Fermi surface states under strains of −4%, 0%, and 4% at $E_F = -0.05$ eV, as shown in Fig. 6. It is evident that compressive (tensile) strain causes the inner electron pockets to expand (shrink), accompanied by the appearance of more (fewer) outer bands on the Fermi surface. Such strain-induced modifications of the Fermi surface significantly influence the k-resolved EE, which is shown in Fig. 7. A similar strain-dependent evolution is observed at $E_F = 0$ eV (Fig. 8), where compressive (tensile) strain induces the expansion (shrinkage) of inner electron pockets and the emergence (reduction) of outer hole pockets, giving rise to the corresponding variation in the k-resolved EE distribution shown in Fig. 9.

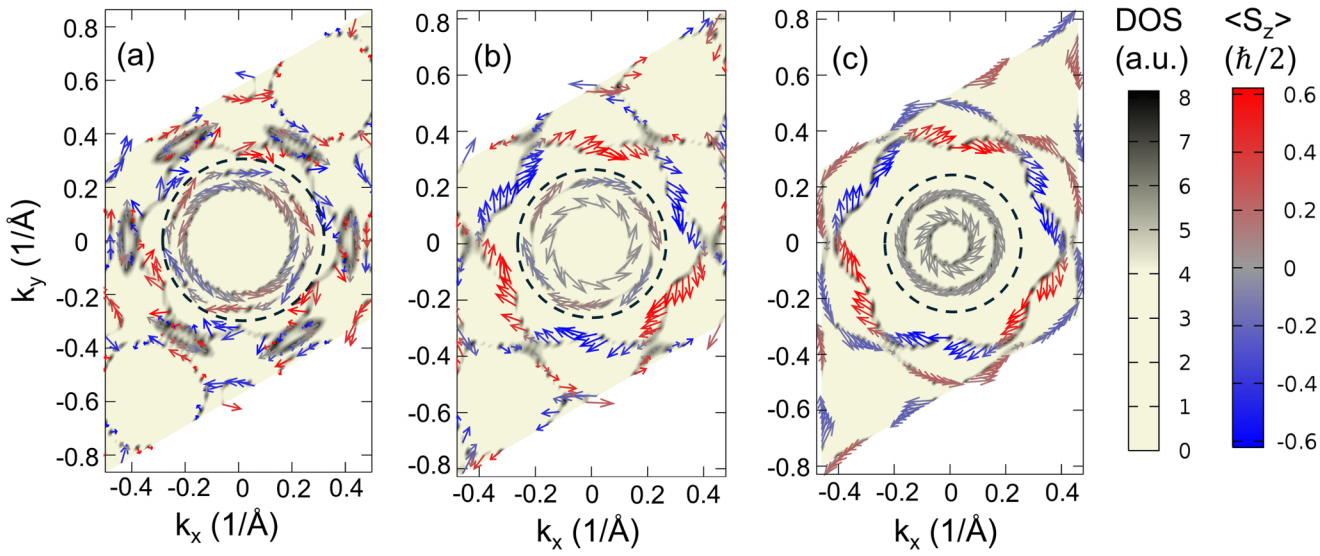

FIG. 6. The Fermi surface states as well as the corresponding spin textures for the $P_\uparrow$ state of monolayer $PtBi_2$ at $E_F = -0.05$ eV with a strain level of (a) -4%, (b) 0%, and (c) 4%. The background color shows the spectral density of the electronic states on the Fermi surface, expressed in arbitrary units. The arrows indicate the direction and magnitude of the in-plane spin expectation values for these Fermi surface states. The color of the arrow represents the expectation value of the out-of-plane spin components. The states from inner electron pockets near the Γ point are circled, while the states outside of the circle are from outer hole pockets.

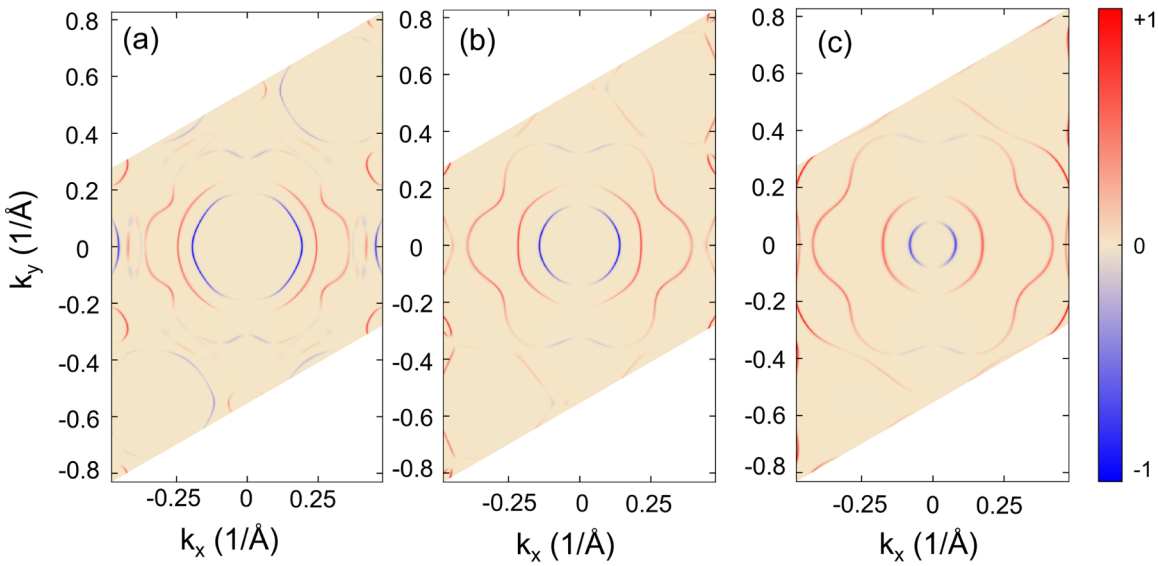

FIG. 7. The **k**-resolved EE coefficient $\chi_{yx}(E_F, \mathbf{k})$ for the $P_\uparrow$ state of monolayer $PtBi_2$ at $E_F = -0.05$ eV under a strain level of (a) -4%, (b) 0%, and (c) 4%. Red and blue denote the positive and negative values of $\chi_{yx}(E_F, \mathbf{k})$, respectively, which have been normalized to the maximum value.

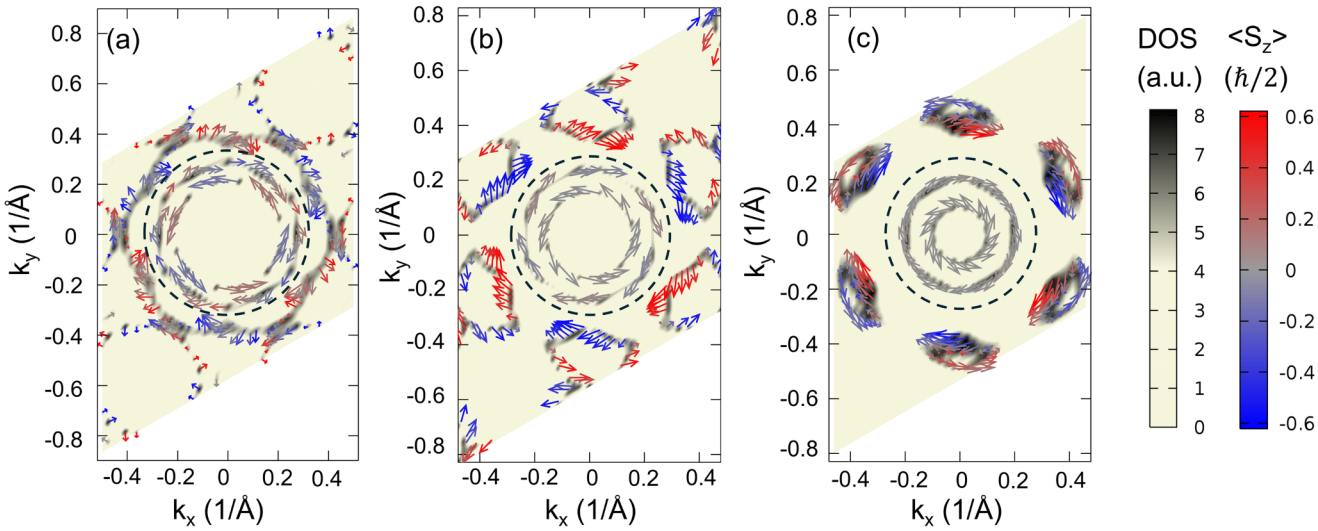

FIG. 8. The Fermi surface states as well as the corresponding spin textures for the $P_\uparrow$ state of monolayer $PtBi_2$ at $E_F = 0$ eV with a strain level of (a) -4%, (b) 0%, and (c) 4%. The background color shows the spectral density of the electronic states on the Fermi surface, expressed in arbitrary units. The arrows indicate the direction and magnitude of the in-plane spin expectation values for these Fermi surface states. The color of the arrow represents the expectation value of the out-of-plane spin components. The states from inner electron pockets near the Γ point are circled, while the states outside of the circle are from outer hole pockets.

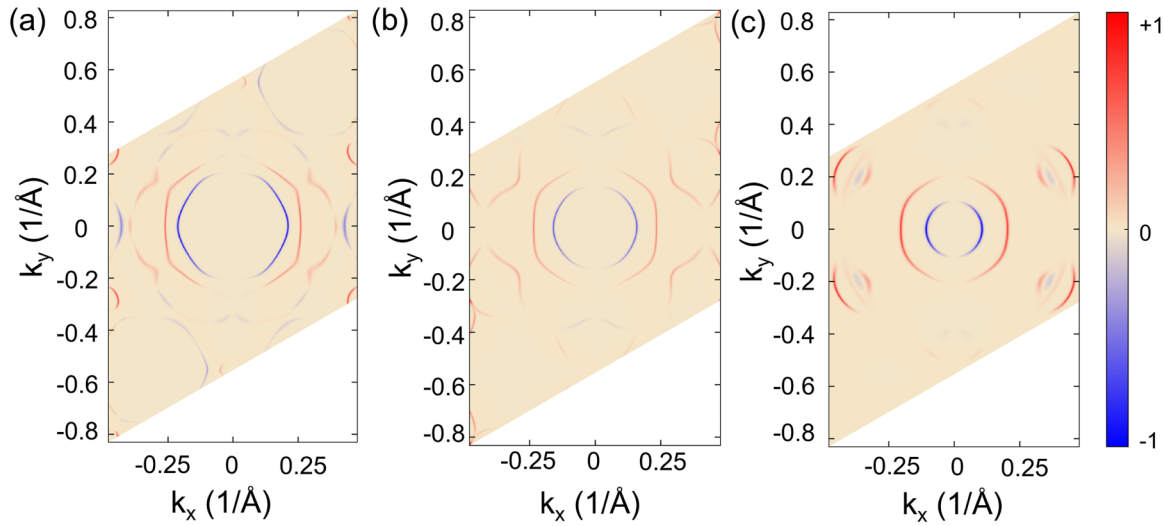

FIG. 9. The **k**-resolved EE coefficient $\chi_{yx}(E_F, \mathbf{k})$ for the $P_\uparrow$ state of monolayer $PtBi_2$ at $E_F = 0$ eV under a strain level of (a) -4%, (b) 0%, and (c) 4%. Red and blue denote the positive and negative values of $\chi_{yx}(E_F, \mathbf{k})$, respectively, which have been normalized to the maximum value.

[1] S. D. Ganichev, E. Ivchenko, V. Bel'Kov, S. Tarasenko, M. Sollinger, D. Weiss, W. Wegscheider, and W. Prettl, Spin-galvanic effect, Nature (London) **417**, 153 (2002).

[2] A. Johansson, Theory of spin and orbital Edelstein effects, J. Phys.: Condens. Matter **36**, 423002 (2024).

[3] H. Xu, J. Zhou, H. Wang, and J. Li, Light-induced static magnetization: Nonlinear Edelstein effect, Phys. Rev. B **103**, 205417 (2021).

[4] S. Lee, D. J. P. de Sousa, Y.-K. Kwon, F. de Juan, Z. Chi, F. Casanova, and T. Low, Charge-to-spin conversion in twisted graphene/WSe_2 heterostructures, Phys. Rev. B **106**, 165420 (2022).

[5] L. A. Benitez, W. Savero Torres, J. F. Sierra, M. Timmermans, J. H. Garcia, S. Roche, M. V. Costache, and S. O. Valenzuela, Tunable room-temperature spin galvanic and spin Hall effects in van der Waals heterostructures, Nat. Mater. **19**, 170 (2020).

[6] H. Yang, B. Martín-García, J. Kimák, E. Schmoranzerová, E. Dolan, Z. Chi, M. Gobbi, P. Němec, L. E. Hueso, and F. Casanova, Twist-angle-tunable spin texture in WSe_2/graphene van der Waals heterostructures, Nat. Mater. **23**, 1502 (2024).

[7] T. Naimer, M. Gmitra, and J. Fabian, Tuning proximity spin-orbit coupling in graphene/$NbSe_2$ heterostructures via twist angle, Phys. Rev. B **109**, 205109 (2024).

[8] K. Zollner, S. M. João, B. K. Nikolić, and J. Fabian, Twist- and gate-tunable proximity spin-orbit coupling, spin relaxation anisotropy, and charge-to-spin conversion in heterostructures of graphene and transition metal dichalcogenides, Phys. Rev. B **108**, 235166 (2023).

[9] L. Salemi, M. Berritta, and P. M. Oppeneer, Quantitative comparison of electrically induced spin and orbital polarizations in heavy-metal/3*d*-metal bilayers, Phys. Rev. Mater. **5**, 074407 (2021).

[10] H. Nakayama, Y. Kanno, H. An, T. Tashiro, S. Haku, A. Nomura, and K. Ando, Rashba-Edelstein magnetoresistance in metallic heterostructures, Phys. Rev. Lett. **117**, 116602 (2016).

[11] G. Lazrak, B. Göbel, A. Barthélémy, I. Mertig, A. Johansson, and M. Bibes, Boosting the Edelstein effect of two-dimensional electron gases by ferromagnetic exchange, Phys. Rev. Res. **6**, 023074 (2024).

[12] S. Varotto, A. Johansson, B. Göbel, L. M. Vicente-Arche, S. Mallik, J. Bréhin, R. Salazar, F. Bertran, P. L. Fèvre, N. Bergeal, *et al.*, Direct visualization of Rashba-split bands and spin/orbital-charge interconversion at $KTaO_3$ interfaces, Nat. Commun. **13**, 6165 (2022).

[13] D. C. Vaz, P. Noël, A. Johansson, B. Göbel, F. Y. Bruno, G. Singh, S. McKeown-Walker, F. Trier, L. M. Vicente-Arche, A. Sander, *et al.*, Mapping spin–charge conversion to the band structure in a topological oxide two-dimensional electron gas, Nat. Mater. **18**, 1187 (2019).

[14] P. Noël, F. Trier, L. M. Vicente Arche, J. Bréhin, D. C. Vaz, V. Garcia, S. Fusil, A. Barthélémy, L. Vila, M. Bibes, *et al.*, Non-volatile electric control of spin–charge conversion in a $SrTiO_3$ Rashba system, Nature (London) **580**, 483 (2020).

[15] Y. Ando, T. Hamasaki, T. Kurokawa, K. Ichiba, F. Yang, M. Novak, S. Sasaki, K. Segawa, Y. Ando, and M. Shiraishi, Electrical detection of the spin polarization due to charge flow in the surface state of the topological insulator $Bi_{1.5}Sb_{0.5}Te_{1.7}Se_{1.3}$, Nano Lett. **14**, 6226 (2014).

[16] C. Li, O. Van 'T Erve, J. Robinson, Y. Liu, L. Li, and B. Jonker, Electrical detection of charge-current-induced spin polarization due to spin-momentum locking in Bi_2Se_3, Nat. Nanotechnol. **9**, 218 (2014).

[17] M. A. Hoque, L. Sjöström, D. Khokhriakov, B. Zhao, and S. P. Dash, Room temperature nonlocal detection of charge-spin interconversion in a topological insulator, npj 2D Mater. Appl. **8**, 10 (2024).

[18] E. Barts, K. Tenzin, and J. Sławińska, Efficient spin accumulation carried by slow relaxons in chiral tellurium, Nat. Commun. **16**, 4056 (2025).

[19] F. Calavalle, M. Suárez-Rodríguez, B. Martín-García, A. Johansson, D. C. Vaz, H. Yang, I. V. Maznichenko, S. Ostanin, A. Mateo-Alonso, A. Chuvilin, *et al.*, Gate-tuneable and chirality-dependent charge-to-spin conversion in tellurium nanowires, Nat. Mater. **21**, 526 (2022).

[20] K. Tenzin, A. Roy, F. T. Cerasoli, A. Jayaraj, M. B. Nardelli, and J. Sławińska, Collinear Rashba-Edelstein effect in nonmagnetic chiral materials, Phys. Rev. B **108**, 245203 (2023).

[21] S. Varotto, L. Nessi, S. Cecchi, J. Sławińska, P. Noël, S. Petrò, F. Fagiani, A. Novati, M. Cantoni, D. Petti, *et al.*, Room-temperature ferroelectric switching of spin-to-charge conversion in germanium telluride, Nat. Electron. **4**, 740 (2021).

[22] J. Li, A. H. Comstock, A. McConnell, X. Li, Y. Yun, D. Sun, and X. Xu, Giant interfacial spin Hall angle from Rashba-Edelstein effect revealed by the spin Hall Hanle process, Phys. Rev. B **108**, L241403 (2023).

[23] K. Tenzin, A. Roy, H. Jafari, B. Banas, F. T. Cerasoli, M. Date, A. Jayaraj, M. Buongiorno Nardelli, and J. Sławińska, Analogs of Rashba-Edelstein effect from density functional theory, Phys. Rev. B **107**, 165140 (2023).

[24] H. Jafari, A. Roy, and J. Sławińska, Ferroelectric control of charge-to-spin conversion in WTe_2, Phys. Rev. Mater. **6**, L091404 (2022).

[25] B. Zhao, B. Karpiak, D. Khokhriakov, A. Johansson, A. M. Hoque, X. Xu, Y. Jiang, I. Mertig, and S. P. Dash, Unconventional charge–spin conversion in Weyl-semimetal WTe_2, Adv. Mater. **32**, 2000818 (2020).

[26] A. Popoola, R. Kashikar, A. Azmy, I. Spanopoulos, H. Jafari, J. Sławińska, S. Witanachchi, S. Lisenkov, and I. Ponomareva, Mechanically and electrically tunable Rashba-Edelstein effect in ferroelectric semiconductors, $CsGeX_3$ (X = I, Br, Cl), Phys. Rev. Mater. **9**, 084412 (2025).

[27] S. Leiva-Montecinos, L. Vojáček, J. Li, M. Chshiev, L. Vila, I. Mertig, and A. Johansson, Current-induced spin and orbital polarization in the ferroelectric Rashba semiconductor GeTe, Phys. Rev. Res. **7**, 043329 (2025).

[28] M. Milivojević, J. Mnich, P. Jureczko, M. Kurpas, and M. Gmitra, Ferroelectric switching control of spin current in graphene proximitized by In_2Se_3, Mater. Futures **5**, 015201 (2026).

[29] P. W. Anderson and E. I. Blount, Symmetry considerations on martensitic transformations: "Ferroelectric" metals? Phys. Rev. Lett. **14**, 217 (1965).

[30] Z. Fei, W. Zhao, T. A. Palomaki, B. Sun, M. K. Miller, Z. Zhao, J. Yan, X. Xu, and D. H. Cobden, Ferroelectric switching of a two-dimensional metal, Nature (London) **560**, 336 (2018).

[31] Y. Shi, Y. Guo, X. Wang, A. J. Princep, D. Khalyavin, P. Manuel, Y. Michiue, A. Sato, K. Tsuda, S. Yu, *et al.*, A ferroelectric-like structural transition in a metal, Nat. Mater. **12**, 1024 (2013).

[32] L. Yang, L. Li, Z.-M. Yu, M. Wu, and Y. Yao, Two-dimensional topological ferroelectric metal with giant shift current, Phys. Rev. Lett. **133**, 186801 (2024).

[33] C. Q. Xu, X. Z. Xing, X. Xu, B. Li, B. Chen, L. Q. Che, X. Lu, J. Dai, and Z. X. Shi, Synthesis, physical properties, and band structure of the layered bismuthide $PtBi_2$, Phys. Rev. B **94**, 165119 (2016).

[34] Q. Yao, Y. P. Du, X. J. Yang, Y. Zheng, D. F. Xu, X. H. Niu, X. P. Shen, H. F. Yang, P. Dudin, T. K. Kim, M. Hoesch, I. Vobornik, Z.-A. Xu, X. G. Wan, D. L. Feng, and D. W. Shen, Bulk and surface electronic structure of hexagonal structured $PtBi_2$ studied by angle-resolved photoemission spectroscopy, Phys. Rev. B **94**, 235140 (2016).

[35] G. Shipunov, I. Kovalchuk, B. R. Piening, V. Labracherie, A. Veyrat, D. Wolf, A. Lubk, S. Subakti, R. Giraud, J. Dufouleur, S. Shokri, F. Caglieris, C. Hess, D. V. Efremov, B. Büchner, and S. Aswartham, Polymorphic $PtBi_2$: Growth, structure, and superconducting properties, Phys. Rev. Mater. **4**, 124202 (2020).

[36] S. Changdar, O. Suvorov, A. Kuibarov, S. Thirupathaiah, G. Shipunov, S. Aswartham, S. Wurmehl, I. Kovalchuk, K. Koepernik, C. Timm, *et al.*, Topological nodal *i*-wave superconductivity in $PtBi_2$, Nature (London) **647**, 613 (2025).

[37] L. Z. Tan and A. M. Rappe, Enhancement of the bulk photovoltaic effect in topological insulators, Phys. Rev. Lett. **116**, 237402 (2016).

[38] P. Giannozzi, S. Baroni, N. Bonini, M. Calandra, R. Car, C. Cavazzoni, D. Ceresoli, G. L. Chiarotti, M. Cococcioni, I. Dabo, *et al.*, QUANTUM ESPRESSO: A modular and open-source software project for quantumsimulations of materials, J. Phys.: Condens. Matter **21**, 395502 (2009).

[39] J. P. Perdew, K. Burke, and M. Ernzerhof, Generalized gradient approximation made simple, Phys. Rev. Lett. **77**, 3865 (1996).

[40] P. E. Blöchl, Projector augmented-wave method, Phys. Rev. B **50**, 17953 (1994).

[41] A. A. Mostofi, J. R. Yates, Y.-S. Lee, I. Souza, D. Vanderbilt, and N. Marzari, Wannier90: A tool for obtaining maximally-localised Wannier functions, Comput. Phys. Commun. **178**, 685 (2008).

[42] Q. Wu, S. Zhang, H.-F. Song, M. Troyer, and A. A. Soluyanov, Wanniertools: An open-source software package for novel topological materials, Comput. Phys. Commun. **224**, 405 (2018).

[43] J. Zelezny, Wannier linear response, https://bitbucket.org/zeleznyj/wannier-linear-response/wiki/Home.

[44] F. Freimuth, S. Blügel, and Y. Mokrousov, Spin-orbit torques in Co/Pt(111) and Mn/W(001) magnetic bilayers from first principles, Phys. Rev. B **90**, 174423 (2014).

[45] M. Hu, O. Janson, C. Felser, P. McClarty, J. van den Brink, and M. G. Vergniory, Spin Hall and Edelstein effects in chiral non-collinear altermagnets, Nat. Commun. **16**, 8529 (2025).

[46] W. Zhang, M. Zheng, Y. Liu, P. Zhang, Z. Zhang, R. Xiong, and Z. Lu, Unconventional spin Hall effect in rutile $Cr_{0.5}X_{0.5}O_2$ (X = Ti, V, Os, Fe), Phys. Rev. B **110**, 214419 (2024).

[47] K. Yang, Y. Wang, and C.-X. Liu, Momentum-space spin antivortex and spin transport in monolayer Pb, Phys. Rev. Lett. **128**, 166601 (2022).

[48] R. Feng, Y. Zhang, J. Li, Q. Li, C. Bao, H. Zhang, W. Chen, X. Tang, K. Yaegashi, K. Sugawara, *et al.*, Giant Rashba splitting in PtTe/$PtTe_2$ heterostructure, Nat. Commun. **16**, 2667 (2025).

[49] W. Yao, E. Wang, H. Huang, K. Deng, M. Yan, K. Zhang, K. Miyamoto, T. Okuda, L. Li, Y. Wang, *et al.*, Direct observation of spin-layer locking by local Rashba effect in monolayer semiconducting $PtSe_2$ film, Nat. Commun. **8**, 14216 (2017).

[50] S. LaShell, B. A. McDougall, and E. Jensen, Spin splitting of an Au(111) surface state band observed with angle resolved photoelectron spectroscopy, Phys. Rev. Lett. **77**, 3419 (1996).

[51] Y. M. Koroteev, G. Bihlmayer, J. E. Gayone, E. V. Chulkov, S. Blügel, P. M. Echenique, and P. Hofmann, Strong spin-orbit splitting on Bi surfaces, Phys. Rev. Lett. **93**, 046403 (2004).

[52] P. D. C. King, R. C. Hatch, M. Bianchi, R. Ovsyannikov, C. Lupulescu, G. Landolt, B. Slomski, J. H. Dil, D. Guan, J. L. Mi, *et al.*, Large tunable Rashba spin splitting of a two-dimensional electron gas in Bi_2Se_3, Phys. Rev. Lett. **107**, 096802 (2011).

[53] H. Yi, L.-H. Hu, Y. Wang, R. Xiao, J. Cai, D. R. Hickey, C. Dong, Y.-F. Zhao, L.-J. Zhou, R. Zhang, *et al.*, Crossover from Ising-to Rashba-type superconductivity in epitaxial Bi_2Se_3/monolayer $NbSe_2$ heterostructures, Nat. Mater. **21**, 1366 (2022).

[54] G. Bihlmayer, P. Noël, D. V. Vyalikh, E. V. Chulkov, and A. Manchon, Rashba-like physics in condensed matter, Nat. Rev. Phys. **4**, 642 (2022).

[55] K. Abdukayumov, O. Paull, M. Mičica, F. Ibrahim, L. Vojáček, A. Wright, S. Massabeau, F. Mazzola, V. Polewczyk, C. Jego, *et al.*, Monolayer control of spin-charge conversion in van der Waals heterostructures, Phys. Rev. Lett. **135**, 016702 (2025).

[56] R. González-Hernández, P. Ritzinger, K. Výborný, J. Železný, and A. Manchon, Non-relativistic torque and Edelstein effect in non-collinear magnets, Nat. Commun. **15**, 7663 (2024).

[57] A. Chakraborty, A. Birk Hellenes, R. Jaeschke-Ubiergo, T. Jungwirth, L. Šmejkal, and J. Sinova, Highly efficient non-relativistic Edelstein effect in nodal *p*-wave magnets, Nat. Commun. **16**, 7270 (2025).

[58] X. Xi, H. Berger, L. Forró, J. Shan, and K. F. Mak, Gate tuning of electronic phase transitions in two-dimensional $NbSe_2$, Phys. Rev. Lett. **117**, 106801 (2016).

[59] D. García Ovalle, A. Pezo, and A. Manchon, Spin-orbit torque for field-free switching in C_{3v} crystals, Phys. Rev. B **107**, 094422 (2023).

[60] S. Vajna, E. Simon, A. Szilva, K. Palotas, B. Ujfalussy, and L. Szunyogh, Higher-order contributions to the Rashba-Bychkov effect with application to the Bi/Ag(111) surface alloy, Phys. Rev. B **85**, 075404 (2012).

[61] J.-J. Xian, C. Wang, J.-H. Nie, R. Li, M. Han, J. Lin, W.-H. Zhang, Z.-Y. Liu, Z.-M. Zhang, M.-P. Miao, *et al.*, Spin mapping of intralayer antiferromagnetism and field-induced spin reorientation in monolayer $CrTe_2$, Nat. Commun. **13**, 257 (2022).

[62] L. Wu, L. Zhou, X. Zhou, C. Wang, and W. Ji, In-plane epitaxy-strain-tuning intralayer and interlayer magnetic coupling in $CrSe_2$ and $CrTe_2$ monolayers and bilayers, Phys. Rev. B **106**, L081401 (2022).

[63] C. Zhao, M. Hu, J. Qin, B. Xia, C. Liu, S. Wang, D. D. Guan, Y. Li, H. Zheng, J. Liu, and J. Jia, Strain tunable semimetal–topological-insulator transition in monolayer $1T'$-WTe_2, Phys. Rev. Lett. **125**, 046801 (2020).

[64] X. Li, H. Chen, and Q. Niu, Out-of-plane carrier spin in transition-metal dichalcogenides under electric current, Proc. Natl. Acad. Sci. USA **117**, 16749 (2020).

[65] J. Sinova, S. O. Valenzuela, J. Wunderlich, C. H. Back, and T. Jungwirth, Spin Hall effects, Rev. Mod. Phys. **87**, 1213 (2015).

[66] D. J. P. de Sousa, S. Lee, Q. Lu, R. G. Moore, M. Brahlek, J.-P. Wang, G. Bian, and T. Low, Ferroelectric semimetals with α-Bi/SnSe van der Waals Heterostructures and Their Topological Currents, Phys. Rev. Lett. **133**, 146605 (2024).

[67] J. Sławińska, F. T. Cerasoli, P. Gopal, M. Costa, S. Curtarolo, and M. Buongiorno Nardelli, Ultrathin SnTe films as a route towards all-in-one spintronics devices, 2D Mater. **7**, 025026 (2020).

[68] H. Wang, P. Gopal, S. Picozzi, S. Curtarolo, M. Buongiorno Nardelli, and J. Sławińska, Spin Hall effect in prototype Rashba ferroelectrics GeTe and SnTe, npj Comput. Mater. **6**, 7 (2020).

[69] J. Qiao, J. Zhou, Z. Yuan, and W. Zhao, Calculation of intrinsic spin Hall conductivity by Wannier interpolation, Phys. Rev. B **98**, 214402 (2018).

[70] I. Žutić, J. Fabian, and S. Das Sarma, Spintronics: Fundamentals and applications, Rev. Mod. Phys. **76**, 323 (2004).